nuclear fusion
IAEA

LETTER • OPEN ACCESS

Three-dimensional nonlinear modeling of ELM dynamics with biasing in HL-3 tokamak

To cite this article: J. Huang *et al* 2025 *Nucl. Fusion* **65** 094001

OPEN ACCESS
IOP Publishing | International Atomic Energy Agency
Nuclear Fusion
Nucl. Fusion **65** (2025) 094001 (9pp)
https://doi.org/10.1088/1741-4326/adfaf4

Letter

Three-dimensional nonlinear modeling of ELM dynamics with biasing in HL-3 tokamak

J. Huang[1], G.Z. Hao[1,*], Y. Suzuki[2], Y.Q. Liu[3], J.X. Li[1], Z.J. Li[1], T.F. Sun[1], B.T. Cui[1], H.K. Yin[1], L. Wang[1], H.Z. Zhao[1], X.Q. Ji[1], W.L. Zhong[1], Y. Liang[4] and HL-3 Team[1]

[1] Southwestern Institute of Physics, PO Box 432, Chengdu 610041, China
[2] Graduate School of Advanced Science and Engineering, Hiroshima University, 739-8572 Higashi-Hiroshima, Japan
[3] General Atomics, PO Box 85608, San Diego, CA 92186-5608, United States of America
[4] Forschungszentrum Jülich GmbH, Institute of Fusion Energy and Nuclear Waste Management, Jülich 52425, Germany

E-mail: haogz@swip.ac.cn

Received 3 June 2025, revised 31 July 2025
Accepted for publication 13 August 2025
Published 22 August 2025

Abstract

The influence of a biased divertor target system on Edge Localized Mode (ELM) dynamics is investigated for the first time in the HL-3 tokamak, focusing on the impact of bias-driven scrape-off layer (SOL) helical currents on three-dimensional (3D) magnetohydrodynamic (MHD) equilibria and instabilities. In a designed 1.6 MA H-mode discharge scenario, the applied SOL currents are modeled as filamentary currents aligned with magnetic field lines near the separatrix, and the resulting 3D perturbed magnetic fields are computed using Biot–Savart law. Nonlinear resistive equilibrium simulations with the HINT code show that the bias-driven currents significantly alter the pressure distribution and magnetic topology near resonant rational surfaces and in the edge stochastic layers, particularly in the pedestal region. Subsequent 3D nonlinear MHD instability analysis using the MIPS code reveals that the growth rate of edge instabilities systematically decreases with increasing SOL current, with a marked reduction observed at 1 kA. Additionally, nonlinear interactions between the external perturbations and intrinsic ballooning modes lead to a redistribution of the mode energy. These results demonstrate the potential of divertor biasing as a viable technique for ELM control in HL-3, offering a promising strategy for controlling edge instabilities and managing heat flux distribution in mega-ampere plasma current H-mode scenarios.

* Author to whom any correspondence should be addressed.

Keywords: edge localized mode, 3D MHD equilibrium, divertor biasing, nonlinear modeling

(Some figures may appear in colour only in the online journal)

1. Introduction

Edge Localized Modes (ELMs) [1, 2] are magnetohydrodynamic (MHD) events that occur in the edge region of a tokamak plasma during high-confinement mode (H-mode) [3], characterized by periodic collapses of the edge pedestal. Each ELM burst is associated with expulsion of large amounts of heat and particles onto the plasma-facing components. The intolerable transient heat loads may ablate the plasma-facing components like divertor plates, leading to a strong reduction of the lifetime [4, 5]. In addition, ELMs might potentially couple or trigger other instabilities, such as the resistive wall mode [6] and the neoclassical tearing mode [7]. The prevention or control of type-I ELMs [8] in H-mode plasma is a big issue for the next generation of fusion devices like ITER [9].

A promising method for ELM control is the application of Resonant Magnetic Perturbations (RMPs) [10]. Generated by specially designed external coils, RMPs have demonstrated effectiveness in a range of devices, including DIII-D [11], JET [12], MAST [13], NSTX [14], ASDEX-Upgrade [15], KSTAR [16], EAST [17] and HL-2A [18]. These experimental findings have positioned RMPs as one of the most promising approaches for ELM control in ITER [19]. RMP penetration can induce magnetic islands on resonant rational surface where $q = m/n$, with q being the safety factor and m, n the poloidal and toroidal mode numbers, respectively. When island chains on adjacent rational surfaces overlap, the magnetic field lines become chaotic [20]. Due to the strong magnetic shear at the plasma edge in divertor configuration with an X-point, island overlap can occur readily, leading to stochastic magnetic field behavior. This stochasticity degrades the edge transport barrier, keeping the plasma in a stable regime with respect to the peeling–ballooning mode [21]. Nevertheless, installing and utilizing RMP coils in a fusion reactor environment is challenging due to space constraints and high neutron fluxes. In parallel, the concept of magnetic perturbations generated by toroidally non-axisymmetric currents in the SOL plasma, induced by biased divertor plates, has been proposed both theoretically and experimentally [22–29], notably in devices like HL-2A [30]. Since the helix of magnetic field lines in the SOL region is close to that in the pedestal region during H-mode, SOL currents aligned with the magnetic field near the plasma edge can also induce RMPs, leading to changes in edge magnetic topology and modifications to ELM behavior. Recently, a divertor biased target system has been designed for the HL-3 tokamak to explore the effects of divertor induced SOL current on plasma behavior. The potential of this biased system for ELM control in H-mode discharges with mega-ampere plasma current should be investigated through modeling.

The modeling of ELM dynamics commonly relies on nonlinear MHD formulations, and several numerical codes have been developed over the past three decades, including JOREK [31, 32], BOUT++ [33], M3D [34, 35], GEMR [36], NIMROD [37], MEGA [38], CLT [39], and MIPS [40]. In this paper, to investigate magnetic perturbations effects on ELM dynamics with 3D MHD equilibrium in finite-β plasmas (where β denotes the ratio of plasma pressure to magnetic pressure), the nonlinear MHD code MIPS, in combination with the HINT code [41, 42], is employed.

The paper is organized as follows. Section 2 introduces the modeling approach for simulating ELM dynamics with a divertor-based target system. Section 3 presents the analysis of 3D MHD equilibrium and ELM behavior with bias-driven SOL current. Conclusions and discussions are provided in section 4.

2. Modeling setup

2.1. Divertor biased target system in HL-3

Built in 2020, the HL-3 tokamak is currently the largest advanced tokamak in China, featuring a major radius $R_0 = 1.78$ m and a minor radius $a = 0.65$ m, with an aspect ratio of 2.8 [43]. Its technical specifications include a toroidal magnetic field (B_T) of 2.2–3 T and a plasma current (I_p) up to 3 MA, with elongation $\kappa \leqslant 1.8$ and triangularity $\delta \leqslant 1.8$. An upper divertor biased target system has been designed with four groups of biasing plates in HL-3. As shown in figure 1(a), there are eight biasing plates located on the upper first wall, with four positioned on the inner side and four on the outer side, uniformly distributed in the toroidal direction. This system can drive currents along magnetic field lines in the SOL region, generating 3D magnetic perturbations similar to those produced by RMP coils. It should be noted that the amplitude of the bias-driven SOL current depends on the plasma voltammetry characteristics, which are determined not only by the external power supply but also strongly influenced by SOL plasma parameters such as plasma density, temperature, and the area of the biased plates. In a typical H-mode discharge in HL-3, the upper limit of the bias-driven SOL current amplitude, approaching the electron saturation current, can reach up to 1.2 kA per plate from theoretical estimation [25]. To validate the feasibility of ELM control, it is essential to investigate both the biasing configuration and, more critically, the dependence of ELM dynamics on the SOL current amplitude through modeling.

2.2. Numerical scheme

The flowchart of the ELM dynamics simulation with biasing is shown in figure 2. The initial two-dimensional (2D) plasma equilibrium is generated using OMFIT [44], based on a 1.6 MA discharge featuring a H-mode pedestal structure and an upper single null (USN) configuration, which provides the

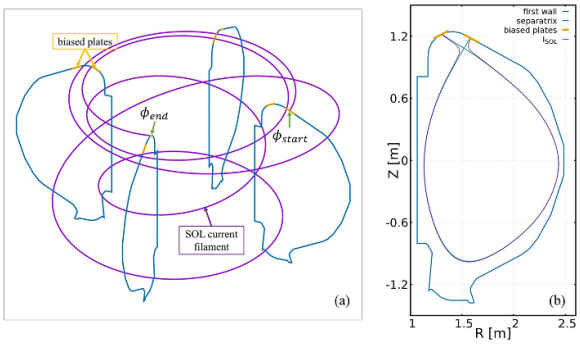

Figure 1. (*a*) 3D view and (*b*) 2D projection of the bias-driven SOL current filament indicated by the thick purple line. The biased plate locations are marked along the orange line.

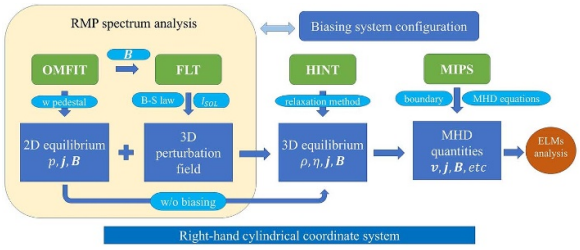

Figure 2. Flowchart of the ELM dynamics simulation process with biasing.

2D plasma parameters for the subsequent analysis. Starting from the 2D magnetic field, a field-line tracing method [19] is applied to simulate the SOL current filaments driven by the external biasing system. As shown in figure 1, subfigure (*a*) provides a 3D view, while subfigure (*b*) presents a 2D projection of the bias-driven SOL current filament. The initial point for field-line tracing is located near the strike point of the upper biased plate. Given the biasing configuration and current filaments, the resulting 3D magnetic perturbations are calculated using Biot–Savart law. To optimize the configuration, the resulting RMP spectrum and the associated magnetic topology in the flux (PEST) coordinate [45, 46] are analyzed. Following the identification of a suitable biasing setup, the impact of the SOL current amplitude on the 3D MHD equilibrium is investigated using the HINT code. Finally, the nonlinear evolution of ELM dynamics is simulated with the MIPS code.

The HINT code solves the 3D nonlinear equilibrium by a two-step relaxation method on a rectangular grid in cylindrical coordinate (R, ϕ, Z), where R and Z denote the horizontal and the vertical directions, respectively, and ϕ is the toroidal angle. In the presented simulation, the grid resolution is set to $512 \times 128 \times 1024$ in the R, ϕ and Z directions. The initial conditions are constructed by superposing the 2D equilibrium pressure, plasma current, and magnetic field with the 3D perturbations generated by the biasing system. Without assuming nested flux surfaces, HINT enables accurate resolution of 3D MHD equilibrium including magnetic islands and stochastic regions. The plasma equilibrium response and the modified magnetic topology are self-consistently obtained upon relaxation to the final 3D equilibrium with the applied biasing in a finite-β plasma.

The MIPS code solves the full set of MHD equations to analyze plasma instability characteristics, utilizing the same cylindrical coordinate system as HINT and based on a finite difference numerical scheme. Initialized with the equilibrium output, time integration is performed via a fourth-order Runge–Kutta scheme to enable the simulation of MHD dynamics through time evolution. In the simulation, the resistivity follows the Spitzer model, scaling with temperature as $T^{-3/2}$. To minimize the influence of artificial boundary effects on edge instabilities, the plasma domain in MIPS is extended slightly beyond the first wall.

3. Numerical results

3.1. Biasing configuration with RMP spectrum analysis

As previously described, four groups of biased plates are designed in HL-3. When both the start and end points of a bias-driven SOL current filament are constrained to the biased plates, three representative biasing configurations with dominate toroidal mode numbers $n = 1$ and 2 can be defined: '$+0-0$', '$++--$' and '$+-+-$'. Here '$+$' denotes a current flowing from the outer to the inner plate (equivalently, a positive bias applied to the outer plate), '$-$' denotes the opposite direction, and '0' indicates that no bias is applied at that plate. The first two configurations correspond to $n = 1$ dominant magnetic perturbations, while the latter correspond to $n = 2$. Other possible configurations, such as '$+000$' and '$+0+0$', are also feasible but produce comparatively weaker resonant effects. To ensure that both endpoints lie on biased plates, the condition $\mathrm{mod}\left(\phi_{\mathrm{start}} - \phi_{\mathrm{end}}, \frac{\pi}{2}\right) = 0$ is imposed, where ϕ_{start} and ϕ_{end} denote the toroidal angles of the start and end points of the current filament, respectively. For the target 2D equilibrium, $\phi_{\mathrm{start}} - \phi_{\mathrm{end}} = \frac{\pi}{2}$, as illustrated in figure 1(*a*), which also allows the endpoints to be positioned as close as possible to the strike points. It is worth noting that, in experimental applications, the biasing configuration can be more flexible than the idealized setup used in this simulation. The current path is not restricted to start and end at specific plates. Instead, the bias current may flow from the vessel wall to a plate or in the opposite direction. Furthermore, different bias voltages can be independently applied to the inner and outer divertor plates, enabling configurations such as 'outer $(+++-)$ inner $(+-++)$' that offer adjustable degrees of freedom to tailor the perturbation characteristics.

To determine an appropriate biasing configuration for subsequent nonlinear simulations, the vacuum RMP spectrum and associated magnetic topology [47] are analyzed. The results indicate that configurations with a greater number of biased plates generate stronger RMPs at a fixed SOL current amplitude. For instance, in the $n = 1$ dominant case, the '$++--$' configuration exhibits a stronger resonant spectrum than the '$+000$' or '$+0-0$' cases. Figure 3 presents the RMP spectra and corresponding Poincaré plots [48] for the '$++--$' and '$+-+-$' configurations, both with a bias-driven SOL

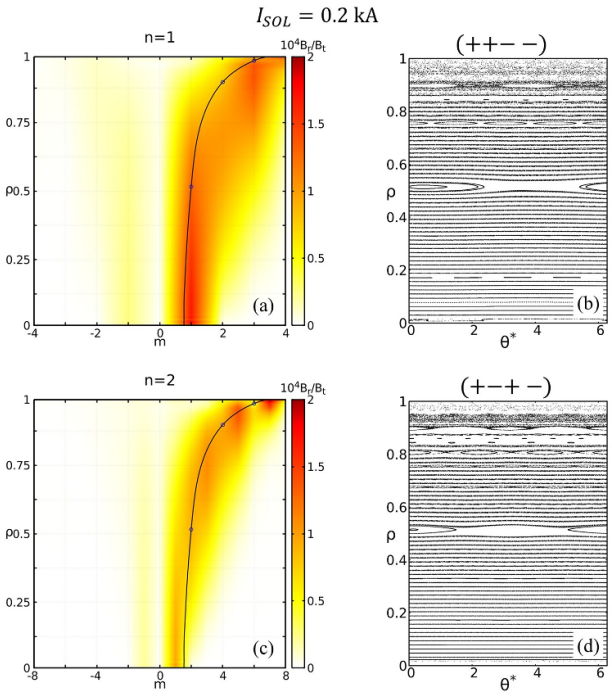

Figure 3. (*a*), (*c*) Resonant component spectra and (*b*), (*d*) Poincaré plots in PEST coordinates for the '$++--$' and '$+-+-$' configurations, for the dominant $n = 1$ (upper panels) and 2 (lower panels) perturbation fields. The black curve represents the safety factor q profile, with blue circles marking the $q =$ 1, 2, and 3 rational surfaces.

current of $I_{\mathrm{SOL}} = 0.2$ kA. While the two configurations show similar resonant strengths near the edge, the '$++--$' case exhibits a slightly enhanced resonant amplitude in the core region. This is reflected in the magnetic island width at the $q = 1$ surface, which scales with the square root of the resonant magnetic field amplitude at the corresponding rational surface, i.e. $\sqrt{B_{\mathrm{r_{m,n}}}}$ and is marginally larger in the '$++--$' case. The level of edge stochasticity is comparable between the two. To ensure adequate edge resonance for modifying the pedestal topology while limiting core perturbations and preserving overall confinement, the '$+-+-$' configuration is selected as the optimal choice for subsequent nonlinear simulations. It is also noted that, in contrast to conventional 3D RMP coils which produce both resonant and non-resonant $(\pm m, n)$ harmonics, the bias-driven helical SOL currents aligned with magnetic field lines predominantly generate (m,n) components, effectively reducing non-resonant contributions or the kink effects.

3.2. 3D equilibrium with biasing

Based on the '$+-+-$' configuration, 3D nonlinear resistive MHD equilibria are calculated with the HINT code for a range of bias-driven SOL current amplitudes. As the perturbated field superimposed, magnetic islands form and the edge magnetic field becomes increasingly stochastic. The pressure profile evolves self-consistently to satisfy the dynamic force balance equation $\vec{J} \times \vec{B} = \nabla p$. Figure 4 presents a comparison of equilibrium pressuredistributions with a bias-driven SOL current of $I_{\mathrm{SOL}} = 0.2$kA across selected toroidal cross-sections, highlighting the 3D structure and significant modifications of edge region. Owing to the $n = 2$ dominant biasing configuration, the resulting pressure and magnetic topology at $\phi = 0$ and $\phi = \pi$ are qualitatively similar. It should be noted that in the Poincaré plots, certain magnetic islands are not fully resolved due to the uniform seeding of field-line tracing points from the magnetic axis to the X-point. For example, the $(m,n) = (2,2)$ magnetic island chain near the original $q = 1$ surface appears partially incomplete (only one island is visible in the plot near the core), as the two islands reside in separate flux tubes under $n = 2$ dominant resonant perturbations.

Figure 5(*a*) shows the toroidally averaged pressure profiles at the midplane for various bias-driven SOL current amplitudes, ranging from 0 kA to 1 kA in 0.2 kA increments. In this work, the pressure is normalized by the on-axis pressure of the equilibrium without biasing unless otherwise specified. Away from resonant rational surfaces, the pressure profiles remain relatively unaffected by the increasing SOL current. While near the resonant surfaces where magnetic islands form, clear pressure flattening is observed. In the pedestal region, significant pressure reduction occurs as the magnetic field becomes stochastic. As SOL current amplitude increases, the pressure modification becomes more pronounced but not in a strictly linear manner. For instance, comparing figures 5(*b*) and (*c*), corresponding to $I_{\mathrm{SOL}} = 0.2$ kA and 0.4 kA respectively, reveals that while the color bar range in figure 5(*c*) is twice that of figure 5(*b*), the blue regions indicating pressure reduction are noticeably deeper and broader, implying a nonlinear effect. As the SOL current approaches 1 kA, the resonance strength further increases, enhancing

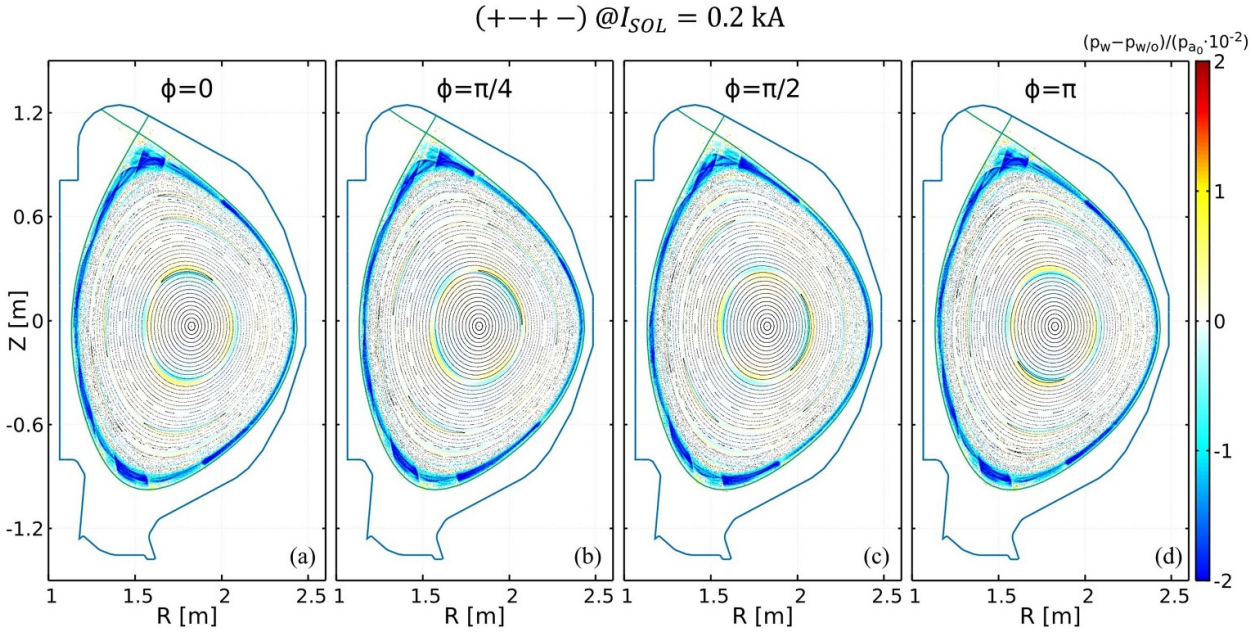

Figure 4. Pressure modifications and Poincaré plots in cylindrical coordinates at selected toroidal cross-sections for the '$+-+-$' configuration with a bias-driven SOL current of $I_{\rm SOL} = 0.2$ kA. p_w and $p_{w/o}$ represent the pressure computed by HINT with and without the biasing SOL current, respectively. p_{a_o} denotes the on-axis pressure of the equilibrium without biasing.

edge stochasticity and resulting in additional flattening and the onset of fluctuations in the pedestal pressure profile. Overall, as the SOL current increases, the pedestal height decreases, with a slight inward shift of the pedestal, particularly for the 0.8 kA and 1 kA cases. These nonlinear 3D MHD equilibria, characterized by substantial modifications of the edge pressure gradient, are expected to strongly affect the characteristics and evolution of edge MHD instabilities.

3.3. Edge instability with biasing

Based on the 3D equilibria generated for various bias-driven SOL current amplitudes, the time evolution of MHD instabilities is investigated by solving the full set of MHD equations using the MIPS code. Figure 6 presents the temporal evolution of the kinetic energy of MHD instabilities. The growth rate of instabilities, reflected by the slope of the curves during the linear phase, generally decreases with increasing SOL current. The evolution of total kinetic energy reveals a delayed onset of instability for most cases, except for the $I_{\rm SOL} = 0.6$ kA case. Although the growth rate in this case is slightly lower than that for $I_{\rm SOL} = 0.4$ kA, the earlier onset may be attributed to a slightly steeper pressure gradient near the pedestal foot, as indicated by the comparison between the green and blue curves in figure 5(*a*). At higher current levels ($I_{\rm SOL} = 0.8$ kA and 1 kA), the pedestal height is substantially reduced, leading to a further decrease in the instability growth rate. Since the MIPS code does not capture the full ELM cycle dynamics, all cases ultimately enter a nonlinear saturation phase, where the total kinetic energy levels off to similar values in logarithmic scale. Notably, when viewed in linear coordinates, the saturated kinetic energy decreases distinctly with increasing SOL current.

To elucidate the instability dynamics, the evolution of mode structures is analyzed using the perturbed pressure distribution and associated magnetic topology in cylindrical coordinates. Figure 7 presents contour plots of the pressure perturbation at the $\phi = 0$ toroidal cross-section, comparing cases without biasing and with a bias-driven SOL current of 0.4 kA. In the natural ELM case (i.e. without biasing), a typical edge ballooning mode develops on the low-field side during the early linear phase ($t = 200\tau_{\rm A}$). As the instability evolves ($t = 250\tau_{\rm A}$), erosion of the edge magnetic surfaces is observed, and by the onset of the nonlinear phase ($t = 300\tau_{\rm A}$), the mode transitions into an interchange-like structure superimposed with ballooning characteristics. With the application of biasing, the amplitude of edge instabilities is significantly reduced, as evidenced by the lower magnitude in the color scale at corresponding time slices. Furthermore, the spatial distribution of the most unstable regions exhibits clear toroidal modulation induced by the applied $n = 2$ dominant perturbation. This modulation is clearly evident when comparing the $\phi = 0$ and $\phi = \pi/2$ cross-sections (figures 7(*b*), (*d*) and (*f*), (*h*)). While the unstable regions remain similar in the natural ELM case, pronounced toroidal asymmetry appears in the biased case, indicating a coupling between the applied perturbation and the evolving edge mode structure.

To further characterize the instability dynamics, the temporal evolution of toroidal mode components of the kinetic energy is examined, as shown in figure 8. In the absence of biasing, high-n modes with the dominant mode at $n = 27$ rapidly emerge during the early linear phase and remain dominant throughout as figure 8(*a*) shows. In contrast, with a bias-driven SOL current of 0.4 kA (figure 8(*b*)), the onset of high-n modes is noticeably delayed, while the evolution of low-n modes proceeds similarly to, or slightly earlier than

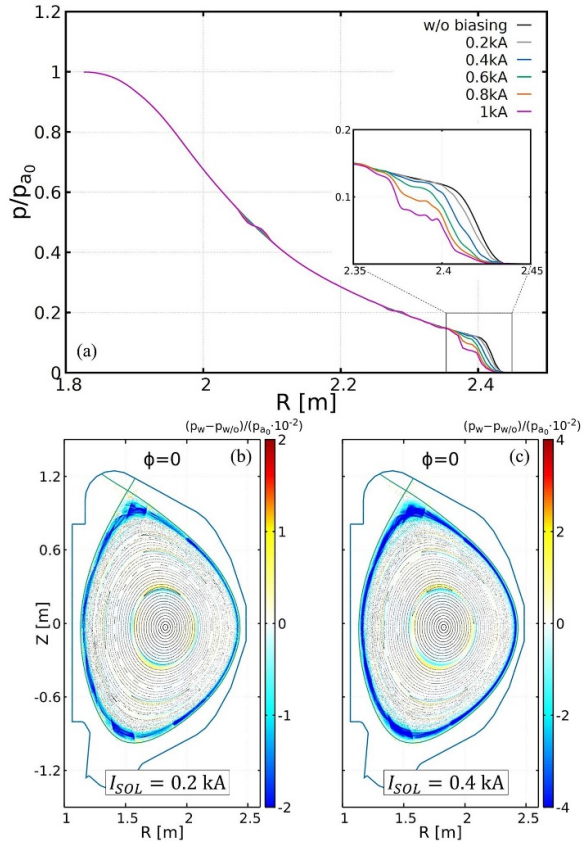

Figure 5. (*a*) The toroidally averaged pressure profiles at the midplane for systematically varied bias-driven SOL current amplitudes, (*b*) and (*c*) the pressure modifications and Poincaré plots at $\phi = 0$ for the '$+-+-$' configuration with a bias-driven SOL current of $I_{\mathrm{SOL}} = 0.2$ kA and 0.4 kA, respectively.

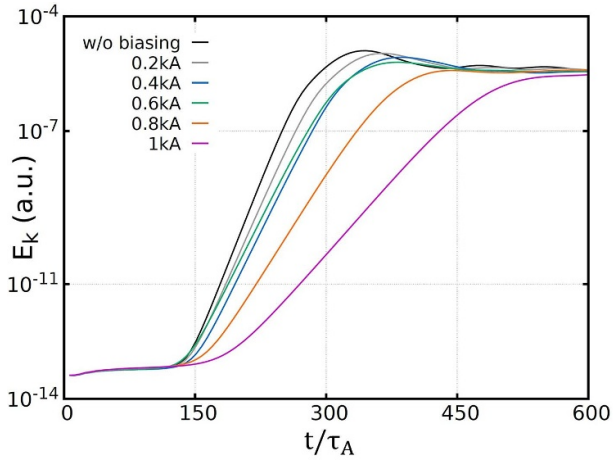

Figure 6. Temporal evolution of the kinetic energy (logarithmic scale) of MHD instabilities for varying bias-driven SOL current amplitudes. Time is normalized to the Alfvén time.

that in the unbiased case. In the nonlinear saturation phase, the $n = 2$ mode becomes dominant, indicating a redistribution of mode energy and reflecting the influence of the externally applied $n = 2$ dominant perturbation on the instability spectrum. Figure 9(*a*) shows the kinetic energy of individual toroidal mode components ($n = 1 - 32$) at the saturation phase ($t = 600\tau_{\mathrm{A}}$). In the absence of biasing, the dominant mode is $n = 27$, whereas for bias-driven SOL currents exceeding 0.4 kA, the peak energy shifts to $n = 2$. This shift highlights the impact of the externally imposed $n = 2$ dominant perturbation, which also enhances the energy content of even-n modes compared to adjacent odd-n components. A possible mechanism for this behavior involves the presence of sideband modes and nonlinear mode coupling effects. For the '$+-+-$' biasing configuration, in addition to the dominant $n = 2$ component, higher-order sidebands such as $n = 6$, 10, and 14 exhibit relatively strong perturbations, whereas the odd-n components are noticeably weaker. Other even-n components, such as $n = 4$, 8, and 12, may be further enhanced through nonlinear coupling between the dominant mode and the relatively strong sidebands. This spectral asymmetry results in a preferential enhancement of even-n modes, particularly in the low-n range. Figure 9(*b*) summarizes the linear growth rates of individual toroidal mode components for different bias-driven SOL current amplitudes. In the natural ELM case, the low-n modes exhibit slightly higher growth rates than the high-n modes, despite their delayed onset, as they ultimately reach comparable amplitudes at nonlinear phase (see figure 8(*a*)). With the application of biasing, the growth rates of different n components tend to remain at a similar level. A general trend of decreasing growth rate with increasing SOL current is observed, except for the $I_{\mathrm{SOL}} = 0.4$ kA and 0.6 kA cases, which show nearly the same values. Given that the estimated bias-driven SOL current can reach up to 1.2 kA per electrode in HL-3, the numerical results presented here suggest that the proposed biasing configuration represents a promising approach for ELM control in HL-3 H-mode discharges with mega-ampere-level plasma currents.

To further assess the applicability of the biasing scheme under ITER-like configuration, simulations were also conducted for a low single null (LSN) configuration with a designed 1.6 MA H-mode discharge in the HL-3 tokamak. Implementing the biasing system in a configuration analogous to the USN case, the results exhibited qualitatively consistent behavior. Figure 10 presents a comparison of the mode structures during the linear phase, both without and with a bias-driven SOL current of 0.4 kA. In the absence of biasing, pronounced edge ballooning structures emerge on the low-field side, indicative of natural ELM onset. When biasing is applied, the amplitude of the pressure perturbation is noticeably reduced, as evidenced by the lower range in the color scale at corresponding time slice. This attenuation in mode strength suggests that the bias-induced perturbation effectively diminishes the growth of edge instabilities during the linear phase. These findings underscore the potential of magnetic perturbations generated by bias-driven SOL currents as a practical approach for ELM control in ITER-like configuration operating in high plasma current H-mode regimes.

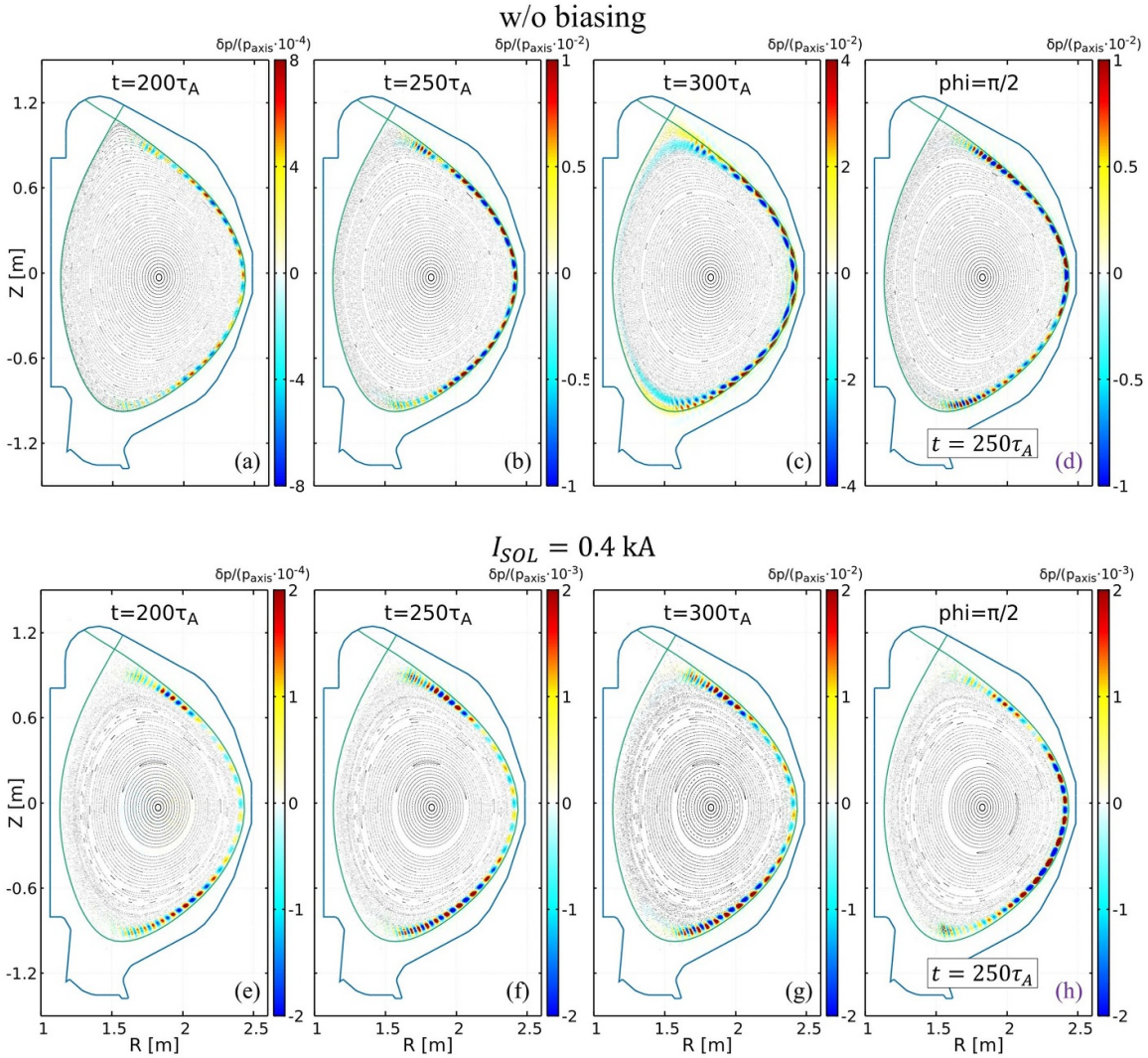

Figure 7. Pressure perturbations at selected time slices for (*a*)–(*c*) unbiased and (*e*)–(*g*) biased ($I_{\mathrm{SOL}} = 0.4$ kA) cases, shown at the $\phi = 0$ toroidal cross-section. Panels (*d*) and (*h*) show corresponding perturbations at $\phi = \pi/2$ for $t = 250\tau_{\mathrm{A}}$ (where τ_{A} is the Alfvén time).

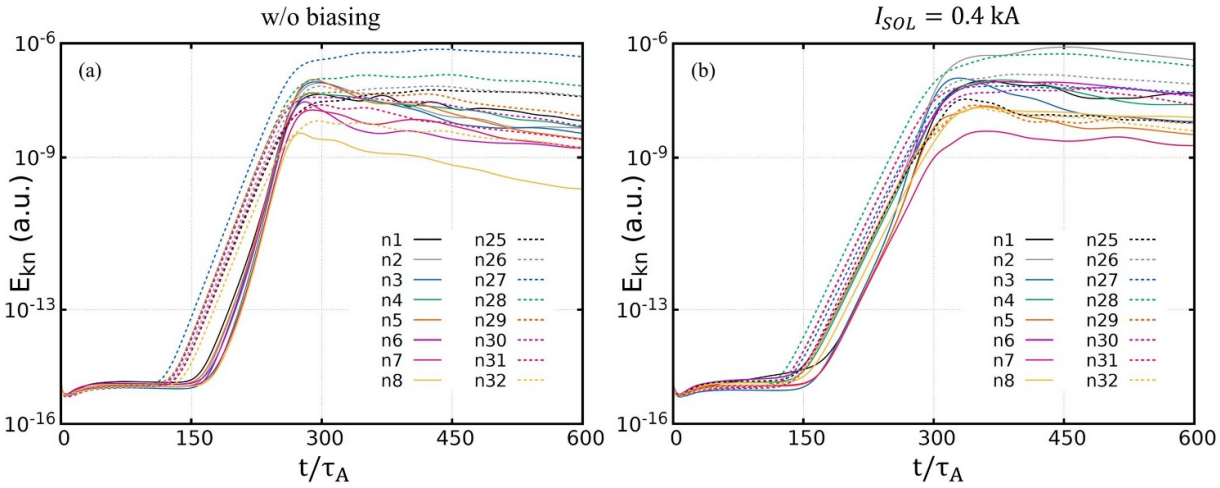

Figure 8. Temporal evolution of toroidal mode-decomposed kinetic energy (logarithmic scale) for (*a*) unbiased and (*b*) biased ($I_{\mathrm{SOL}} = 0.4$ kA) cases.

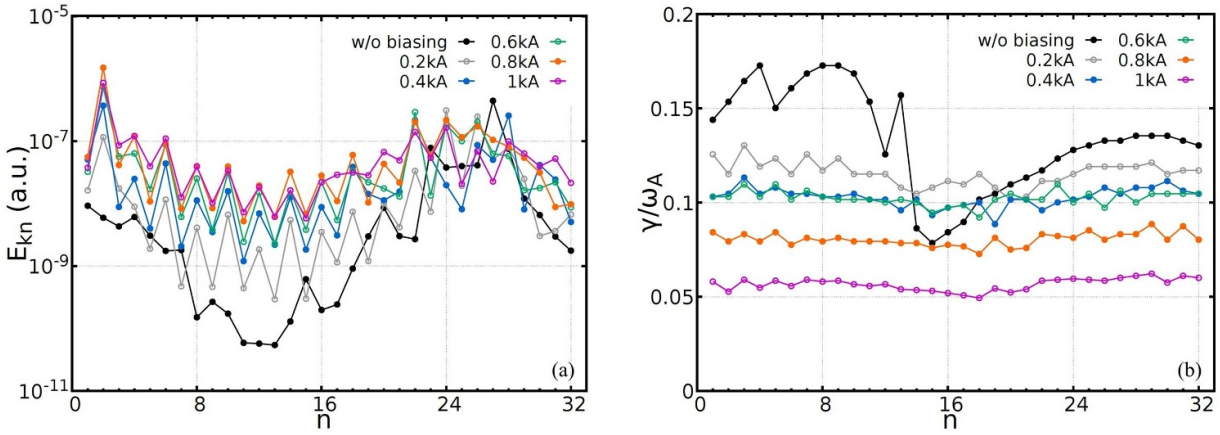

Figure 9. (*a*) Kinetic energy at $t = 600\tau_A$ and (*b*) growth rates for individual toroidal mode components under varying amplitudes of bias-driven SOL current.

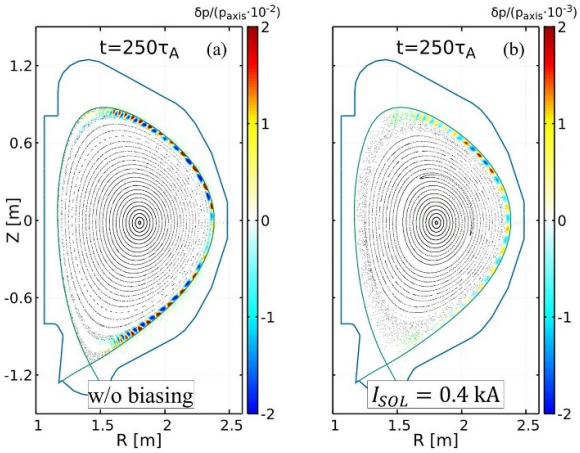

Figure 10. Pressure perturbations at selected time slice for (*a*) unbiased and (*b*) biased ($I_{SOL} = 0.4$ kA) cases, shown at the $\phi = 0$ toroidal cross-section in low single null (LSN) configuration.

4. Conclusion and discussion

This study presents a numerical investigation of ELM dynamics under divertor biasing in HL-3 H-mode plasmas, using the 3D nonlinear HINT and MIPS codes. For a typical 1.6 MA H-mode discharge, the application of a bias-driven SOL current approaching 1 kA per plate as designed leads to a clear modification of pedestal pressure and edge stabilities. These changes are primarily attributed to restructuring of the edge magnetic topology with resonant magnetic field, resulting in reduced pedestal pressure gradient and altered ELM behavior. The findings demonstrate that the proposed biasing configuration may serve as an effective strategy for ELM control in HL-3.

The spectral properties of the biasing-induced magnetic perturbations are analyzed and found to differ from those generated by conventional 3D RMP coils. The biasing system preferentially excites resonant components with minimal non-resonant content. Furthermore, compared to RMP coils, bias-driven SOL current filaments can be located closer to the pedestal region. A relatively small current (∼1 kA in HL-3) can generate comparable edge resonant perturbations to those produced by RMP coils (∼10 kA in HL-3), which may reduce the impact on the core plasma.

The 3D equilibria computed with increasing bias-driven SOL current amplitudes reveal a nonlinear response of the plasma edge, characterized by enhanced magnetic stochasticity and pressure profile modification at higher current levels. These changes are self-consistently balanced by the plasma to maintain MHD force balance. Under experimental conditions, additional complexities may arise due to the finite area of the biased targets, self-induced perturbations of the currents along flux tubes and potential SOL current leakage [29]. A more rigorous simulation of SOL current behavior under biasing would ideally employ a particle-in-cell approach, which demands substantial computational resources. In the present study, a simplified model using a single filament with constant current density per biased plate is employed. Despite its simplicity, this approach successfully captures the essential features of the magnetic topology and edge stochasticity, as the helical structure of field lines remains largely preserved even within stochastic regions. This supports the validity of the model for predictive studies of edge behavior under bias-driven SOL current.

MHD stability analysis using the MIPS code shows that in the absence of biasing, high-*n* ballooning modes emerge early and remain dominant throughout both the linear and nonlinear phases. When biasing is applied, the onset of high-*n* modes is delayed, and the growth rates of all toroidal components are systematically reduced with increasing SOL current. In the nonlinear regime, the externally imposed perturbation redistributes mode energy, leading to a marked enhancement of the $n = 2$ component consistent with the dominant biasing configuration. This nonlinear energy redistribution is qualitatively similar to the behavior observed in RMP simulations using the JOREK code [49]. These findings suggest that the biasing scheme not only suppresses linear growth but also alters the nonlinear dynamics of edge instabilities through mode coupling. In this study, edge instabilities are primarily

dominated by the ballooning branch. For scenarios where peeling mode dominated instabilities are expected, the reduction in pressure gradient induced by biasing can be inferred to result in a corresponding decrease in the bootstrap current contribution, thereby potentially stabilizing the peeling mode. Further detailed investigations will be conducted in future work.

The achievable SOL current amplitude and its effective path length are influenced by multiple factors, including SOL plasma conditions such as density and temperature, as well as parallel and cross-field transport and the connection length of open magnetic field lines. It should also be noted that plasma flow induced screening effects are not considered in the present study. These effects may reduce the degree of edge stochasticity and magnetic island widths. Accurate comparison with experimental data, particularly in validating the SOL current amplitudes and assessing the impact of screening, is essential. Future work will address these aspects by combining experimental observations with resistive MHD response modeling using the MARS-F code [50, 51].

Acknowledgments

This work was supported by the National Magnetic Confinement Fusion Energy R&D Program (Nos. 2022YFE03060002 and 2019YFE03030003), the Youth Science and Technology Innovation team of Sichuan Province (No. 2022JDTD0003), the National Natural Science Foundation of China (Nos. 12375214 and 12475218), the China National Nuclear Corporation Fundamental Research Program (Nos. CNNC-JCYJ-202236 and CNNC-JCYJ-202324), and the Innovation Program of Southwestern Institute of Physics (No. 202301XWCX006-04). Most of the numerical computations were carried out on the Tianhe supercomputing system at the National Supercomputer Center in Tianjin, China.

ORCID iDs

J. Huang 0000-0001-9217-2966
G.Z. Hao 0000-0003-2310-6134
Y. Suzuki 0000-0001-7618-6305
Y.Q. Liu 0000-0002-8192-8411
L. Wang 0009-0007-8193-5658
H.Z. Zhao 0000-0002-8874-3452
W.L. Zhong 0000-0001-8217-9400
Y. Liang 0000-0002-9483-6911

References

[1] Zohm H. 1996 *Plasma Phys. Control. Fusion* **38** 105
[2] Connor J.W. 1998 *Plasma Phys. Control. Fusion* **40** 531
[3] Wagner F. *et al* 1982 *Phys. Rev. Lett.* **49** 1408
[4] Kirk A., Wilson H.R., Counsell G.F., Akers R., Arends E., Cowley S.C., Dowling J., Lloyd B., Price M. and Walsh M. 2004 *Phys. Rev. Lett.* **92** 245002
[5] Leonard A.W. 2014 *Phys. Plasmas* **21** 090501
[6] Igochine V. 2012 *Nucl. Fusion* **52** 074010
[7] King J.D. *et al* 2012 *Phys. Plasmas* **19** 022503
[8] Loarte A. *et al* 2002 *Plasma Phys. Control. Fusion* **44** 1815
[9] Loarte A. *et al* 2007 *Nucl. Fusion* **47** S203
[10] Evans T.E. *et al* 2006 *Nat. Phys.* **2** 419
[11] Evans T.E. *et al* 2004 *Phys. Rev. Lett.* **92** 235003
[12] Liang Y. *et al* 2007 *Phys. Rev. Lett.* **98** 265004
[13] Kirk A. *et al* 2010 *Nucl. Fusion* **50** 034008
[14] Canik J.M. *et al* 2010 *Nucl. Fusion* **50** 034012
[15] Suttrop W. *et al* 2011 *Phys. Rev. Lett.* **106** 225004
[16] Jeon Y.M. *et al* 2012 *Phys. Rev. Lett.* **109** 035004
[17] Sun Y. *et al* 2016 *Phys. Rev. Lett.* **117** 115001
[18] Sun T.F., Liu Y., Ji X.Q., Liu Y.Q., Ke R., Gao J.M., Wu N., Deng W., Xu M. and Duan X.R. 2021 *Nucl. Fusion* **61** 036020
[19] Bécoulet M. *et al* 2008 *Nucl. Fusion* **48** 024003
[20] Ghendrih P., Grosman A. and Capes H. 1996 *Plasma Phys. Control. Fusion* **38** 1653
[21] Snyder P.B. and Wilson H.R. 2003 *Plasma Phys. Control. Fusion* **45** 1671
[22] Cohen R.H. and Ryutov D.D. 1997 *Nucl. Fusion* **37** 621
[23] Fielding S.J., Cohen R.H., Helander P. and Ryutov D.D. 2001 *J. Nucl. Mater.* **290–293** 405
[24] Ryutov D.D., Helander P. and Cohen R.H. 2001 *Plasma Phys. Control. Fusion* **43** 1399
[25] Joseph I., Cohen R.H. and Ryutov D.D. 2009 *Phys. Plasmas* **16** 052510
[26] Counsell G.F. *et al* 2003 *Nucl. Fusion* **43** 1197
[27] Toi K. *et al* 2021 *Plasma Fusion Res.* **16** 2402024
[28] Wang N.C., Song Z., Liang Y., Yang J., Wang T., Zhang H., Chen Z., Yu K. and Ding Y. 2019 *Nucl. Fusion* **59** 096047
[29] Toi K. *et al* 2023 *Nucl. Fusion* **63** 106018
[30] Hao G.Z. *et al* 2023 *Nucl. Fusion* **63** 016006
[31] Huysmans G.T.A. and Czarny O. 2007 *Nucl. Fusion* **47** 659
[32] Becoulet M. *et al* 2022 *Nucl. Fusion* **62** 066022
[33] Xu X.Q., Dudson B., Snyder P.B., Umansky M.V. and Wilson H. 2010 *Phys. Rev. Lett.* **105** 175005
[34] Park W., Belova E.V., Fu G.Y., Tang X.Z., Strauss H.R. and Sugiyama L.E. 1999 *Phys. Plasmas* **6** 1796
[35] Munaretto S., Orlov D.M., Paz-Soldan C., Bykov I., Lasnier C.J., Lyons B.C. and Wang H. 2022 *Nucl. Fusion* **62** 026018
[36] Scott B.D. 2005 *Phys. Plasmas* **12** 102307
[37] Sovinec C.R., Glasser A.H., Gianakon T.A., Barnes D.C., Nebel R.A., Kruger S.E., Schnack D.D., Plimpton S.J., Tarditi A. and Chu M.S. 2004 *J. Comput. Phys.* **195** 355
[38] Todo Y. and Sato T. 1998 *Phys. Plasmas* **5** 1321
[39] Zhang W., Jardin S.C., Ma Z.W., Kleiner A. and Zhang H.W. 2021 *Comput. Phys. Commun.* **269** 108134
[40] Todo Y., Nakajima N., SATO M. and Miura H. 2010 *Plasma Fusion Res.* **5** S2062
[41] Suzuki Y., Nakajima N., Watanabe K., Nakamura Y. and Hayashi T. 2006 *Nucl. Fusion* **46** L19–L24
[42] Suzuki Y. 2017 *Plasma Phys. Control. Fusion* **59** 054008
[43] Duan X.R. *et al* 2024 *Nucl. Fusion* **64** 112021
[44] Meneghini O. *et al* 2015 *Nucl. Fusion* **55** 083008
[45] Grimm R.C., Dewar R.L. and Manickam J. 1983 *J. Comput. Phys.* **49** 94
[46] Huang J., Suzuki Y., Liang Y., Jia M., sun Y., Chu N., Xu J. and Wu M. 2019 *Plasma Sci. Technol.* **21** 065105
[47] Schaffer M.J., Menard J.E., Aldan M.P., Bialek J.M., Evans T.E. and Moyer R.A. 2008 *Nucl. Fusion* **48** 024004
[48] Bazzani A., Malavasi M., Siboni S., Pellacani C., Rambaldi S. and Turchetti G. 1989 *Nuovo Cimento B* **103** 659
[49] Wang L. *et al* 2024 *Nucl. Fusion* **64** 096016
[50] Liu Y.Q., Bondeson A., Fransson C.M., Lennartson B. and Breitholtz C. 2000 *Phys. Plasmas* **7** 3681
[51] Liu Y.Q., Kirk A., Gribov Y., Gryaznevich M.P., Hender T.C. and Nardon E. 2011 *Nucl. Fusion* **51** 083002